

1 <https://doi.org/10.1007/s12583-020-1085-4>

2 **Nitrogen isotopes from the Neoproterozoic Liulaobei Formation, North China:**  
3 **implications for nitrogen cycling and eukaryotic evolution**

4 Ting Yang<sup>1</sup>, Xinqiang Wang<sup>1,2\*</sup>, Dongtao Xu<sup>1</sup>, Xiaoying Shi<sup>1,2</sup>, Yongbo Peng<sup>3,4</sup>

5 <sup>1</sup> *School of Earth Science and Resources, China University of Geosciences (Beijing), Beijing 100083, China*

6 <sup>2</sup> *State Key Laboratory of Biogeology and Environmental Geology, China University of Geosciences (Beijing),*  
7 *Beijing 100083, China*

8 <sup>3</sup> *International Center for Isotope Effect Research, Nanjing University, Nanjing 210023, China*

9 <sup>4</sup> *School of Earth Sciences and Engineering, Nanjing University, Nanjing 210023, China*

10

11 Corresponding author: X Wang, [wxqiang307@126.com](mailto:wxqiang307@126.com)

12

13 **Abstract:** The nitrogen isotope compositions ( $\delta^{15}\text{N}$ ) of sedimentary rocks can provide  
14 information about the nutrient N cycling and redox conditions that may have played  
15 important roles in biological evolution in Earth's history. Although considerable  $\delta^{15}\text{N}$   
16 data for the Precambrian have been published, there is a large gap during the early  
17 Neoproterozoic that restrains our understanding of the linkages among N cycling,  
18 ocean redox changes and biological evolution during this key period. Here, we report  
19 bulk  $\delta^{15}\text{N}$  and organic carbon isotope ( $\delta^{13}\text{C}_{\text{org}}$ ) compositions as well as the total  
20 nitrogen (TN) and total organic carbon (TOC) contents from the Tonian fossiliferous  
21 Liulaobei Formation in the southern part of the North China Platform. The  $\delta^{15}\text{N}$  in the  
22 study section is dominated by very stable values centering around +4.3‰, which is  
23 moderately lower than in modern sediments ( $\sim$  +6‰). These positive  $\delta^{15}\text{N}$  values

24 were attributed to partial denitrification under low primary productivity (scenario 1)  
25 and/or denitrification coupled with dissimilatory nitrate reduction to ammonium  
26 (DNRA) (scenario 2). In either case, the availability of fixed nitrogen may have  
27 provided the nutrient N required to facilitate facilitated eukaryotic growth. Our study  
28 highlights the pivotal role of nutrient N in the evolution of eukaryotes.

29

30 **Key words:** Neoproterozoic, Tonian, Liulaobei Formation, Nitrogen isotopes,  
31 Eukaryotic evolution, Nutrient limitation

32

### 33 **0 INTRODUCTION**

34 The Earth's surface environment underwent significant changes in redox conditions  
35 during the early-middle Neoproterozoic Tonian Period (ca.1000-720 Ma). Model  
36 calculations based on chromium isotope ( $\delta^{53}\text{Cr}$ ) compositions suggest that the  
37 atmospheric oxygen levels were extremely lower during the Mesoproterozoic,  
38 accounting for only <0.1% to 1% of the present atmospheric levels (PAL) (Cole et al.,  
39 2016; Planavsky et al., 2014). This low baseline was interrupted by several short-term  
40 oxygenation events that may have resulted in an increase in the atmospheric oxygen  
41 levels to >1% PAL (Shang et al., 2019; Canfield et al., 2018; Zhang et al., 2018, 2016),  
42 but the nature of these inferred oxygenation events remains a topic of debate (Wang et  
43 al., 2020a; Diamond et al., 2018; Planavsky et al., 2016). A major inflection in the  
44  $\delta^{53}\text{Cr}$  record of marine sediments during the Tonian Period was also taken as evidence  
45 of a significant shift in atmospheric oxygen from the low baseline during the

46 Mesoproterozoic to a relatively high level (but still lower than today), leading up to  
47 the Neoproterozoic oxygenation event (Cole et al., 2016; Planavsky et al., 2014).  
48 Similar redox changes may have also occurred in ocean environments at this time.  
49 There is increasing consensus that the global oceans of the Mesoproterozoic were  
50 characterized by pervasive anoxic conditions (Reinhard et al., 2017, 2013; Lyons et al.,  
51 2014; Sahoo et al., 2012; Planavsky et al., 2011; Poulton and Canfield, 2011; Scott et  
52 al., 2008). A common ocean redox structure is the widespread occurrence of euxinic  
53 wedges along the productive continental margin between layers of ferruginous  
54 seawater ('sandwich' model) (Planavsky et al., 2011; Poulton and Canfield, 2011).  
55 The rise in atmospheric oxygen levels during the early-middle Neoproterozoic would  
56 have led to the expansion of oxic seawater, with chemocline possibly down to below  
57 the storm wave base or even the intermittent oxygenation of the deep ocean, as  
58 evidenced by the widespread deposition of sulfate evaporites (Turner and Bekker,  
59 2016), and the pronounced enrichment of some redox sensitive elements (e.g., Mo, U,  
60 V) in the euxinic shale of the Wynniatt Formation (Thomson et al., 2015), which is  
61 indicative of large seawater reservoirs of these elements in well-oxygenated oceans.  
62 This inference is further supported by the long-term trends in phosphorus (P)  
63 concentrations in fine-grained siliciclastic rocks showing a marked increase between  
64 ca. 800-700 Ma (Reinhard et al., 2017) (but see Guilbaud et al.(2020) for a different  
65 idea) as well as the increase in the ratios of iodine-to-calcium-magnesium [ $I/(Ca+Mg)$ ]  
66 at ca. 800 Ma (Lu et al., 2017). Alternatively, Guilbaud et al. (2015) argued that the  
67 global ocean evolved from the Mesoproterozoic sandwich model to dominantly

68 ferruginous conditions during the early Neoproterozoic. The remarkable change in the  
69 redox conditions of the atmosphere-ocean system during the early-middle  
70 Neoproterozoic broadly coincided with the increasing diversification of eukaryotic  
71 macro- and microfossils (Li et al., 2020; Tang et al., 2020; Xiao and Tang, 2018;  
72 Knoll and Nowak, 2017), likely suggesting a causal relationship between them.

73 Nitrogen is one of the major nutrient elements in oceans that is required for all  
74 living organisms (e.g., Tyrrell, 1999). The availability of nutrient N in oceans has an  
75 important regulatory effect on primary production, which can affect the ocean redox  
76 conditions and provides the foundational food and energy sources for life at higher  
77 trophic levels. Conversely, the amount and speciation of nutrient N are largely  
78 dependent on the ocean redox landscape (Ader et al., 2016; Stüeken et al., 2016) and  
79 can be affected by the variations in primary production (Lam and Kuypers, 2011;  
80 Sigman et al., 2009; Altabet, 2006). These complex interactions, coupled with  
81 characteristic nitrogen isotope fractionations associated with specific pathways in the  
82 N cycle (e.g., Stüeken et al., 2016; Sigman et al., 2009), render the nitrogen isotope  
83 composition ( $\delta^{15}\text{N}$ ) in sedimentary rocks as an effective proxy that has been widely  
84 used to trace the evolution of N cycling and ocean redox conditions during critical  
85 intervals in Earth history (e.g., Chang et al., 2019; Chen et al., 2019; Ossa Ossa et al.,  
86 2019; Kipp et al., 2018; Wang et al., 2018a, 2018b; Luo et al., 2018, 2011; Zerkle et  
87 al., 2017; Stüeken et al., 2015; Higgins et al., 2012). Unfortunately, the roles of the N  
88 cycle in the redox shift and eukaryotic diversification in the Tonian has not been  
89 adequately investigated. Currently, nitrogen isotope studies from the early-middle

90 Neoproterozoic have only been reported from the ca. 800 Ma Callanna Group, South  
91 Australia, which has experienced extensive metamorphism up to amphibolite  
92 (Stüeken et al., 2019), and the ca. 750 Ma Russøya Member of the Elbobreen  
93 Formation in northeast Svalbard (Ader et al., 2014). More  $\delta^{15}\text{N}$  data are needed from  
94 Tonian sedimentary rocks with low metamorphic grades on other continents.

95 Here, we conducted a systematic study of  $\delta^{15}\text{N}$  and  $\delta^{13}\text{C}_{\text{org}}$  in the Tonian Liulaobei  
96 Formation in the Huainan Group, Anhui Province. This unit contains abundant micro-  
97 and microfossils including cyanobacteria and diverse eukaryotes (Pang et al., 2018;  
98 Tang et al., 2017, 2013; Xiao et al., 2014; Dong et al., 2008; Yin and Sun, 1994; Sun  
99 et al., 1986; Yin, 1985; Wang et al., 1984), and has been subjected to integrated  
100 geochemical studies of iron (Fe) speciation, sulfur isotopes ( $\delta^{34}\text{S}$ ) of both pyrite and  
101 carbonate-associated sulfate (CAS),  $\delta^{13}\text{C}_{\text{org}}$  and carbonate carbon isotopes ( $\delta^{13}\text{C}_{\text{carb}}$ ),  
102 as well as P speciation (Guilbaud et al., 2020, 2015). Combined with these  
103 paleontological and geochemical data, the new  $\delta^{15}\text{N}$  and  $\delta^{13}\text{C}_{\text{org}}$  values will be used to  
104 address the nitrogen cycling and its potential relationship with ocean redox change  
105 and eukaryotic diversification in this critical interval.

106

## 107 **1 GEOLOGICAL SETTING**

108 The study area (Huainan) is located on the southern margin of the North China  
109 Platform (Fig. 1B). Newly published paleomagnetic data indicate that the North China  
110 Platform was located in the lower middle latitudes ( $\sim 30^\circ\text{N}$ ) of the North Hemisphere  
111 during the early Neoproterozoic (Fig. 1A; Zhao et al., 2020). The Neoproterozoic

112 strata in the Huainan area include, in ascending order, the Huainan Group, the Feishui  
113 Group, and the Fengtai Formation (Fig. 2; Tang et al., 2013 and references therein).  
114 The Huainan Group unconformably overlies the Paleoproterozoic-Mesoproterozoic  
115 basement and can be subdivided into the lower Caodian and Bagongshan Formations,  
116 which consist mainly of conglomerate and quartz sandstone, and the upper Liulaobei  
117 Formation which is dominated by gray shale with subordinate argillaceous limestone  
118 and siltstone (Fig. 2). Abundant fossils, including *Tawuia*, *Chuarua*,  
119 *Trachyhystrichosphaera*, *Sinosabellidites*, acritarchs, filamentous cyanobacteria, and  
120 possible vase-shaped microfossils, have been documented from the Liulaobei  
121 Formation (Pang et al., 2018; Tang et al., 2017, 2013; Xiao et al., 2014; Dong et al.,  
122 2008; Yin and Sun, 1994; Sun et al., 1986; Yin, 1985; Wang et al., 1984). The  
123 overlying Feishui Group is characterized by siliciclastic rocks in the lower part  
124 (sandstone of the Shouxian Formation) and carbonate in the middle-upper part  
125 (argillaceous and stromatolitic limestone of the Jiuliqiao Formation and stromatolitic  
126 dolostone of the Sidingshan Formation) (Fig. 2). Macroscopic carbonaceous  
127 compression fossils of *Chuarua*, *Tawuia*, *Sinosabellidites*, *Pararenicola*, and  
128 *Protoarenicola*, as well as possible vase-shaped microfossils, have also been reported  
129 from the Jiuliqiao Formation (Dong et al., 2008; Hong et al., 2004; Zang and Walter,  
130 1992; Sun et al., 1986; Wang et al., 1984). Recently, some calcified cyanobacteria and  
131 viral-like particles were identified in columnar stromatolites of this unit (Lan et al.,  
132 2020). The glacial deposit of the Fengtai Formation (Wang et al., 1984), thought to be  
133 time-equivalent to the late Ediacaran glacial diamictites along the southern margin of

134 the North China Platform (Shen et al., 2010; Xiao et al., 2004), unconformably  
135 overlies the Feishui Group and is in turn unconformably overlain by the Cambrian  
136 Houjiashang Formation (Fig. 2).

137 No reliable radiometric ages have been reported for the Huainan and Feishui  
138 groups due to the lack of volcanic ash layers, but they are loosely constrained by some  
139 Rb–Sr and K–Ar ages to be largely deposited in the Tonian period (ca. 900-750 Ma)  
140 (see summary in Dong et al., 2008) as well as a few detrital U-Pb ages (< 1120 Ma)  
141 (Zhao et al., 2020 and references therein). Cryogenian and Ediacaran ages have also  
142 been suggested for the Huainan and Feishui groups (Xing, 1989), which, however, are  
143 inconsistent with recent paleontological studies (Tang et al., 2013; Dong et al., 2008).  
144 For example, the occurrence of *Trachyhystrichosphaera aimika* in the Liulaobei  
145 Formation favors a Tonian age because all reliable *T. aimika* specimens were reported  
146 from pre-Cryogenian Neoproterozoic rocks (Tang et al., 2013). *T. aimika* was also  
147 reported from the Gouhou Formation in the adjacent Huaibei area (Xiao et al., 2014),  
148 which bears a prominent negative  $\delta^{13}\text{C}_{\text{carb}}$  excursion that could be correlated with the  
149 Bitter Spring anomaly (Xiao et al., 2014). Accepting this correlation scheme, the  
150 Liulaobei Formation in the Huainan area may be constrained to < 820 Ma, given the  
151 age constraints on the Bitter Spring excursion (ca. < 811-780 Ma; Rooney et al., 2014;  
152 Macdonald et al., 2010) and the Gouhou Formation (< 820 Ma; Yang et al., 2012).  
153 Admittedly, this is still an open question for investigation.

154 Our samples were collected from a quarry near Liulaobei Village (116°46'5.79"E,  
155 32°37'40.40" N), where only the upper part of the Liulaobei Formation is well

156 preserved (Fig. 1C). The lower part of the section consists mainly of gray-greenish  
157 shale (Figs. 2 and 3A) with sporadic argillaceous limestone and siltstone. Siltstone  
158 becomes more abundant upsection and even occurs interlayered with gray shale (Fig.  
159 3B). The top of the study section is dominated by argillaceous limestone, silty  
160 limestone intercalated with shale and mudstone (Fig. 3C). Abundant macroscopic  
161 carbonaceous compression fossils were observed in the gray shale of the study section.  
162 The excellent preservation of carbonaceous fossils and the general lack of  
163 wave-agitated sedimentary structures indicate that the Liulaobei Formation was likely  
164 deposited in a relatively deep water environment, possibly below the storm wave base  
165 with a good connection to the open ocean (Guilbaud et al., 2015; Tang et al., 2013).

166

## 167 **2 ANALYTICAL METHOD**

168 Forty-six shale samples from the upper Liulaobei Formation were analyzed for  
169 their  $\delta^{15}\text{N}$  and  $\delta^{13}\text{C}_{\text{org}}$  compositions and their total nitrogen (TN) content, and total  
170 organic carbon (TOC) contents. Fresh sample chips without any weathering surfaces  
171 or visible veins were ground into homogeneous powders below 200 mesh in an agate  
172 mortar. The sample powders were decarbonated with 2 M hydrochloric acid. The  
173 carbonate-free residue was then rinsed with deionized water and centrifuged several  
174 times until a near-neutral pH value was reached. After drying in an oven, powder  
175 samples of approximately 50-100 mg were weighed and wrapped in tin capsules for  
176 analysis. The isotopic and elemental compositions were measured using a Vario  
177 Microcube Elemental Analyzer (EA) connected to an Isoprime 100 isotope ratio mass

178 spectrometer (IRMS) in the Oxy-Anion Stable Isotope Consortium (OASIC) at  
179 Louisiana State University (LSU). The nitrogen isotope compositions are reported in  
180 standard  $\delta$  notation in per mil (‰) deviations from atmospheric N<sub>2</sub> (0‰, Air). The  
181 organic carbon isotope compositions are reported as  $\delta$  values with reference to the  
182 Vienna Pee Dee Belemnite standard (VPDB). The reference standard  
183 acetanilide-OASIC ( $\delta^{13}\text{C} = -27.62\text{‰}$ ,  $\delta^{15}\text{N} = +1.61\text{‰}$ ) was used to calibrate the  
184 analytical results. The reproducibility monitored by the reference was better than 0.1‰  
185 for  $\delta^{13}\text{C}_{\text{org}}$  and 0.3‰ for  $\delta^{15}\text{N}$ .

186

### 187 **3 RESULTS**

188 The analytical results for  $\delta^{15}\text{N}$ ,  $\delta^{13}\text{C}_{\text{org}}$ , TN, and TOC are shown in Fig. 2 and  
189 supplementary Table A1. The  $\delta^{13}\text{C}_{\text{org}}$  values range between -30.55‰ and -28.14‰ in  
190 the study section and show an overall increasing trend upsection (Fig. 2). The  
191 magnitude of variation in all the  $\delta^{13}\text{C}_{\text{org}}$  data is less than 2.5‰. Our data are consistent  
192 with previously published  $\delta^{13}\text{C}_{\text{org}}$  values from the upper Liulaobei Formation  
193 (Guilbaud et al., 2020). The average  $\delta^{13}\text{C}_{\text{org}}$  values from two independent studies  
194 overlapped within their uncertainties ( $-29.46 \pm 0.60\text{‰}$ ,  $n = 46$  vs.  $-28.60 \pm 0.74\text{‰}$ ,  $n =$   
195 31). The  $\delta^{15}\text{N}$  values in the study section are very stable and do not show any  
196 stratigraphic trends (Fig. 2). Most  $\delta^{15}\text{N}$  data fall in a very narrow range between +4.0‰  
197 and +4.5‰, with an average value of  $+4.29 \pm 0.13\text{‰}$  ( $n = 46$ ), which is close to that  
198 of modern seawater ( $\sim +5\text{‰}$ ) (Sigman et al., 2009). The Liulaobei shale samples have  
199 low TOC between 0.05% and 0.17% in the study section, with an average of  $0.11 \pm$

200 0.03% (n = 46), similar to the results reported by Guilbaud et al. (2015). The TN  
201 values range from 0.04% to 0.09%, with an average of  $0.07 \pm 0.02\%$  (n = 46). Both  
202 the TOC and TN show a gradual decreasing trends upsection (Fig. 2). Most of our  
203 samples have molar C/N ratios centering at 2 (Fig. 2), which is significantly lower  
204 than the Redfield ratio (~6.6) (Planavsky, 2014).

205

## 206 **4 DISCUSSION**

### 207 **4.1 The Fidelity of the Primary Isotopic Signals**

208 The bulk  $\delta^{15}\text{N}$  and  $\delta^{13}\text{C}_{\text{org}}$  in sedimentary rocks are potential influenced by  
209 diagenesis, metamorphism and the addition of allochthonous sources (Ader et al.,  
210 2016; Stüeken et al., 2016; Jiang et al., 2012). These effects should be carefully  
211 evaluated before any environmental explanation. The excellent preservation of  
212 abundant carbonaceous compression fossils and other fossils in the Huainan and  
213 Feishui groups (e.g., Xiao et al., 2014; Tang et al., 2013; Dong et al., 2008) indicates a  
214 very low metamorphic grade of the Neoproterozoic succession in the study area. The  
215 isotopic alteration of both  $\delta^{15}\text{N}$  and  $\delta^{13}\text{C}_{\text{org}}$  in sedimentary rocks is generally  $<2\%$  for  
216 metamorphic grades below greenschist (Stüeken et al., 2016; Ader et al., 2016, 2009).  
217 The magnitude of  $\delta^{13}\text{C}_{\text{org}}$  variations (4‰) in the Liulaobei Formation (Fig. 4A;  
218 Guilbaud et al., 2020; this study) cannot be explained by the metamorphic effect.  
219 However, the limited variations in  $\delta^{15}\text{N}$  in the study section (Fig. 2) are within the  
220 range of isotopic alteration by metamorphism and could be caused by this effect. Even  
221 if this is the case, the metamorphic effect on our  $\delta^{15}\text{N}$  is negligible and does not affect

222 the following interpretation.

223 The decomposition of organic matter during diagenesis would also cause the loss of  
224 both C and N from the system. A negative correlation between  $\delta^{13}\text{C}_{\text{org}}$  and TOC (Fig.  
225 4A) may imply the preferential loss of  $^{12}\text{C}$  and a decrease in the C/N ratio ( $\sim 2$ ) (Fig.  
226 2). However, previous study demonstrated that this effect is unlikely to be larger than  
227 2‰ (Ader et al., 2009), which cannot explain the large  $\delta^{13}\text{C}_{\text{org}}$  variations (up to 4‰)  
228 observed in the Liulaobei Formation (Fig. 4A). The nitrogen isotopic fractionation  
229 associated with this process could be high (up to 4‰) when the bottom water was  
230 oxic, but it was low ( $\leq 1\text{--}2\text{‰}$ ) when the sediments were deposited in anoxic  
231 environments (e.g., Prokopenko et al., 2006; Lehmann et al., 2002; Freudenthal et al.,  
232 2001; Altabet et al., 1999). Current Fe speciation data indicate that the Liulaobei  
233 Formation was deposited under anoxic conditions (Guilbaud et al., 2015); therefore,  
234 our  $\delta^{15}\text{N}$  data were not significantly affected by diagenesis. Based on the low TOC,  
235 low pyrite concentrations and high Fe (oxyhydr)oxide contents in the Liulaobei shale,  
236 Guilbaud et al.(2020) also argued that the microbial recycling of organic carbon  
237 during early diagenesis, if any, was likely limited. Furthermore, the  $\delta^{15}\text{N}$  in the study  
238 section did not show a significant correlation with TN or C/N (Fig. 4C and 4D),  
239 suggesting that the  $\delta^{15}\text{N}$  variations were not dependent on the changes in TN and  
240 C/N during diagenesis. The  $\delta^{15}\text{N}$  of sedimentary organic matter may show large  
241 differences from that in the sinking particles at sites off continental margins due to  
242 the extended remineralization of organic matter in the water column (Robinson et al.,  
243 2012). The study section, however, was deposited on a shallow continental margin

244 (Guilbaud et al., 2015), minimizing the effect of this process.

245 Nitrogen in sediments is mainly present in two forms: organic-bound nitrogen and  
246 clay-bound nitrogen (mainly as  $\text{NH}_4^+$ ) (see reviews in Ader et al., 2016; Stüeken et al.,  
247 2016). Clay-bound  $\text{NH}_4^+$  generally comes from the *in situ* deamination of organic  
248 nitrogen, but in some cases it may have additional origins from terrestrial inputs  
249 and/or diagenetic fluids (e.g., Luo et al., 2018). The strong positive correlation  
250 between TOC and TN ( $R^2 = 0.7$ ) in our samples indicates that the analyzed N was  
251 mainly from the organic matter. The nonzero intercept of the TN axis (Fig. 4B)  
252 implies the presence of some clay-bound N in our samples. However, this is unlikely  
253 to cause a large bias in our  $\delta^{15}\text{N}$  data because the  $\delta^{15}\text{N}$  values do not show a  
254 significant difference between high-TN samples (lower part of section) and low-TN  
255 samples (upper part of section) (*t*-test,  $p > 0.05$ ). The addition of detrital organic N  
256 could also affect the primary sedimentary  $\delta^{15}\text{N}$ , especially in the organic-lean  
257 sedimentary rocks as our samples. The current data do not provide convincing  
258 evidence against inputs of detrital organic-bound N, but the low C/N as documented  
259 in our samples has so far not been reported from the old rocks in North China.  
260 Furthermore, it is likely that detrital organic matter would display different C/N ratios  
261 and thus manifest itself as perturbations in the TOC-versus-TN crossplot (Wang et al.,  
262 2020b), which was not the case in our samples (Fig. 4B). In summary, the  $\delta^{15}\text{N}$  and  
263  $\delta^{13}\text{C}_{\text{org}}$  values in the study section recorded near-primary signals and can be used to  
264 extrapolate environmental significance. All  $\delta^{13}\text{C}_{\text{org}}$  values from the Liulaobei  
265 Formation are  $> -31\%$ , and the differences between  $\delta^{13}\text{C}_{\text{carb}}$  and  $\delta^{13}\text{C}_{\text{org}}$  fall between

266 28‰ and 31‰ (Guilbaud et al., 2020), suggesting that the organic matter mainly  
267 originated from the primary productivity (Luo et al., 2014; Hayes et al., 1999). Below,  
268 we mainly focus on the discussion of nitrogen isotopes.

269

#### 270 **4.2 Interpreting the Positive $\delta^{15}\text{N}$ in the Liulaobei Formation**

271 The  $\delta^{15}\text{N}$  from the upper Liulaobei Formation in the study section shows  
272 persistently positive values (average  $+4.29 \pm 0.13\text{‰}$ ,  $n = 46$ ), which are moderately  
273 lower than the mean  $\delta^{15}\text{N}$  ( $\sim +6.0\text{‰}$ ) of modern sediments (Fig. 5). Surprisingly, the  
274 average  $\delta^{15}\text{N}$  of our data, within uncertainties, is indistinguishable from that (average  
275  $+4.36 \pm 0.35\text{‰}$ ,  $n=3$ ) reported from the ca. 750 Ma Russøya Member of the  
276 Elbobreen Formation in northeast Svalbard (Ader et al., 2014), possibly suggesting  
277 that it may represent the signal of the global ocean. The major source of the oceanic N  
278 is biological  $\text{N}_2$  fixation, which generally imparts limited isotopic fractionation and  
279 generates N species with an isotopic composition similar to, or rarely lower than, that  
280 of atmospheric  $\text{N}_2$  ( $-2$  to  $+1\text{‰}$ ) (Zhang et al., 2014). The positive  $\delta^{15}\text{N}$  values  
281 observed in the Liulaobei Formation required the preferential loss of  $^{14}\text{N}$  to oceanic N  
282 sinks. Denitrification (coupled with anammox), the main pathway of the oceanic N  
283 sink, is responsible for the positive  $\delta^{15}\text{N}$  in modern seawater ( $\sim +5\text{‰}$ ) (Sigman et al.,  
284 2009) and has been invoked to explain the positive  $\delta^{15}\text{N}$  in the geological records (Xu  
285 et al., 2020; Chen et al., 2019; Kipp et al., 2018; Luo et al., 2018; Wang et al., 2018a,  
286 2018b, 2013; Koehler et al., 2017; Zerkle et al., 2017; Ader et al., 2014; Algeo et al.,  
287 2014; Stüeken, 2013). Under anoxic conditions, ammonium rather than nitrate may be

288 the dominant dissolved species in seawater, and positive  $\delta^{15}\text{N}$  values could also be  
289 produced through assimilation of  $^{15}\text{N}$ -enriched residual ammonium after  $\text{NH}_4^+$  was  
290 partially utilized elsewhere (Papineau et al., 2009) and partial nitrification followed  
291 by quantitative denitrification (or anammox) (Thomazo et al., 2011). Partial  $\text{NH}_4^+$   
292 assimilation would separate the negative and positive  $\delta^{15}\text{N}$  phases and create large  
293 isotopic fluctuations and spatial variability across the basin (Stüeken, 2013; Papineau  
294 et al., 2009). We tentatively ruled out this possibility since no negative  $\delta^{15}\text{N}$  values  
295 were obtained from the early-middle Neoproterozoic in the study section. Admittedly,  
296 more  $\delta^{15}\text{N}$  data from equivalent strata are required to test this explanation. Several  
297 lines of evidence also argue against partial nitrification as a possible explanation. First,  
298 ammonium is readily oxidized to nitrite and nitrate by nitrification in the presence of  
299 nanomolar levels of dissolved oxygen (e.g., Bristow et al., 2016). Quantitative  
300 nitrification was documented even under suboxic conditions near the chemocline in  
301 the modern Black Sea (Fuchsman et al., 2008). As a corollary, it should also occur in  
302 the similar conditions of the Neoproterozoic oceans. Second, partial nitrification  
303 would result in a very large range in the  $\delta^{15}\text{N}$  data (Wang et al., 2020b; Morales et al.,  
304 2014; Stüeken, 2013) because this mechanism lacks a long-term sink of isotopically  
305 light N from the ocean, which is inconsistent with the very stable  $\delta^{15}\text{N}$  values in our  
306 section (Fig. 2).

307 The preferential removal of  $^{14}\text{N}$  from the ocean by denitrification may provide a  
308 viable explanation for the positive  $\delta^{15}\text{N}$  in the Liulaobei Formation. This scenario  
309 would require that the reduction of nitrate was not quantitative. In modern oceans,

310 partial denitrification occurs in oxygen minimum zones (OMZs) because they only  
311 cover a small portion of the global ocean volume (<0.05%; Lam and Kuypers, 2011),  
312 and nitrate is actively supplied by nitrification in the largely oxic oceans.  
313 Denitrification is commonly quantitative at the chemocline of stratified basins such as  
314 the Black Sea and the Cariaco Basin (Fuchsman et al., 2008; Thunell et al., 2004).  
315 However, partial denitrification could also be possible in a stratified ocean even with  
316 a small nitrate pool if the primary productivity were low. For example, the positive  
317  $\delta^{15}\text{N}$  values in the Mesoproterozoic Gaoyuzhuang Formation were interpreted as  
318 resulting from partial denitrification associated with low primary productivity (Wang  
319 et al., 2020b). This scenario can also be applied to the Liulaobei  $\delta^{15}\text{N}$  record in the  
320 study section (Fig. 6A). The phosphorus speciation data from the Liulaobei Formation  
321 imply a decline in primary productivity due to the substantial sequestration of P by Fe  
322 minerals (Guilbaud et al., 2020). Instead, widespread sulfate evaporites (Turner and  
323 Bekker, 2016), the increase in  $\delta^{53}\text{Cr}$  at ca.900-800 Ma (Cole et al., 2016; Planavsky et  
324 al., 2014), the strong enrichment of Mo in the Wynniatt euxinic shale (Thomson et al.,  
325 2015) and the positive I/(Ca+Mg) excursion at ca. 800 Ma (Lu et al., 2017) suggest a  
326 rise of oxygen in the atmosphere-ocean system and accordingly the increases in  
327 primary productivity and organic burial during this period, which are also supported  
328 by recent model calculations (Crockford et al., 2019).

329 Alternatively, the positive  $\delta^{15}\text{N}$  values from the Liulaobei Formation can be  
330 explained by the involvement of dissimilatory nitrate reduction to ammonium  
331 (DNRA). The end product of DNRA is  $\text{NH}_4^+$  rather than  $\text{N}_2$ . Thus, it is an important

332 biogeochemical process that alleviates oceanic fixed N loss from canonical  
333 denitrification. In some modern coastal settings, DNRA is thought to be responsible  
334 for ~30% of all nitrate reduction (Giblin et al., 2013). The isotopic fractionation  
335 associated with DNRA has not been well constrained, but may be similar to  
336 denitrification with the residual nitrate becoming heavier (McCready et al., 1983).  
337 Assuming that nitrate was reduced exclusively by DNRA in a basin, the sediment  
338  $\delta^{15}\text{N}$  would be close to N fixation (~0 ‰) if  $^{15}\text{N}$ -depleted  $\text{NH}_4^+$  and  $^{15}\text{N}$ -enriched  
339  $\text{NO}_3^-$  were assimilated at the same site on a short-term scale or would show large  
340 temporal and spatial variations (with both negative and positive values) across the  
341 basin if the assimilation of  $^{15}\text{N}$ -depleted  $\text{NH}_4^+$  and  $^{15}\text{N}$ -enriched  $\text{NO}_3^-$  occurred at  
342 different localities. Where nitrate is reduced by both denitrification and DNRA, the  
343 rate of denitrification generally outcompetes that of DNRA due to the large free  
344 energy yield (Lam and Kuypers, 2011). Under such circumstances, denitrification  
345 preferentially releases  $^{14}\text{N}$  to the atmosphere, leaving the residual fixed N species  
346 ( $\text{NH}_4^+$  and/or  $\text{NO}_3^-$ ) enriched in  $^{15}\text{N}$ . The quantitative assimilation of this residual  
347  $^{15}\text{N}$ -enriched nutrient N would transfer the positive  $\delta^{15}\text{N}$  signal to sediments. The  
348 electron donors used for the nitrate reduction (denitrification and DNRA) include  
349 organic matter, ferrous Fe (II) and hydrogen sulfide ( $\text{H}_2\text{S}$ ) (Michiels et al., 2017).  
350 Incubation experiments indicated that DNRA is active in the modern ferruginous  
351 Kabuno Bay in East Africa (Michiels et al., 2017). The early Neoproterozoic may  
352 mark an important transition in the ocean redox structure from the sandwich model to  
353 dominantly ferruginous conditions (Guilbaud et al., 2015). Hence, denitrification

354 coupled with DNRA in the ferruginous ocean provides an alternative explanation for  
355 the persistently positive  $\delta^{15}\text{N}$  values in the Liulaobei Formation (Fig. 6B). Although  
356 this explanation remains speculative due to the lack of convincing evidence for  
357 DNRA, we cannot completely rule out the possibility based on the current data. The  
358 positive  $\delta^{15}\text{N}$  data from the Paleoproterozoic succession in the Animikie Basin, North  
359 America (Godfrey et al., 2013) have been inferred to have resulted from a similar  
360 mechanism (Michiels et al., 2017).

361

### 362 **4.3 Implications for Eukaryotic Evolution**

363 Abundant eukaryotic fossils have been reported from the Liulaobei Formation,  
364 including *Chuarina*, *Tawuia*, *Sinosabellidites*, *Trachyhystrichosphaera*, organic-walled  
365 microfossils, and some possible vase-shaped microfossils (e.g., Tang et al., 2017,  
366 2013; Xiao et al., 2014; Dong et al., 2008; Yin and Sun, 1994; Sun et al., 1986; Yin,  
367 1985; Wang et al., 1984). These fossils show global distribution in the Neoproterozoic  
368 Tonian successions and have the potential to be used for biostratigraphic correlation  
369 across different continents (Riedman and Sadler, 2018; Tang et al., 2013). Their  
370 widespread occurrence likely represents the early stage of extended eukaryotic  
371 diversification from the early Neoproterozoic to the early Cambrian (Xiao and Tang,  
372 2018; Knoll and Nowak, 2017). This biological event was broadly concurrent with the  
373 rise in oxygen levels in the atmosphere-ocean system during the early Neoproterozoic  
374 (Cole et al., 2016; Turner and Bekker, 2016; Thomson et al., 2015; Lyons et al., 2014;  
375 Planavsky et al., 2014), suggesting a linkage between them. Ocean detoxification

376 from the H<sub>2</sub>S-rich shelf margin to dominantly ferruginous conditions was proposed as  
377 an alternative cause of the eukaryotic diversification in this period (Guilbaud et al.,  
378 2015).

379 The  $\delta^{15}\text{N}$  results reported here provide insight into the connection between N  
380 cycling and eukaryotic evolution during the early Neoproterozoic. As discussed in  
381 Section 5.2, the positive  $\delta^{15}\text{N}$  values from the Liulaobei Formation were interpreted as  
382 partial denitrification and/or denitrification coupled with DNRA (Fig. 6). The first  
383 scenario implies low primary productivity, possibly caused by P limitation (Guilbaud  
384 et al., 2020), such that nitrate was able to accumulate in the surface waters. In the  
385 second scenario, DNRA may have played an important role in alleviating nutrient N  
386 loss from a stratified, ferruginous ocean even if primary productivity were elevated.  
387 Either way, the availability of fixed N provided the nutrient N source required for  
388 eukaryotic algae, as they are incapable of directly using atmosphere N<sub>2</sub> through N  
389 fixation. Although the scarcity of P due to the widespread ferruginous conditions in  
390 the early Neoproterozoic (Guilbaud et al., 2020) would inevitably exert environmental  
391 stress on eukaryotic evolution. Early primary producers may be more adaptive to  
392 P-stressed environments (Planavsky, 2014). This inference may be supported by the  
393 relatively high N/P<sub>org</sub> (average ca. 30, based on a preliminary calculation using our  
394 TN data and the P<sub>org</sub> reported in Guilbaud et al., 2020). Hence, we highlight the  
395 pivotal role of bioavailable N in eukaryotic evolution during the early Neoproterozoic.

396

397 **5 CONCLUSIONS**

398 High resolution  $\delta^{15}\text{N}$ ,  $\delta^{13}\text{C}_{\text{org}}$  TN, and TOC data were reported from the upper  
399 Liulaobei Formation in the Huainan area, Anhui Province, with the aim of revealing  
400 the linkages among nitrogen cycling, ocean redox changes and biological evolution  
401 during the early Neoproterozoic. The  $\delta^{15}\text{N}$  in the study section shows stable values  
402 (average  $+4.29 \pm 0.13\%$ ) that are close to the mean  $\delta^{15}\text{N}$  of modern seawater. The  
403 positive  $\delta^{15}\text{N}$  values were interpreted to be the result of partial denitrification under  
404 low primary productivity (scenario 1) and/or denitrification coupled with DNRA  
405 (scenario 2). The current evidence does not completely rule out either of these two  
406 possibilities. Nevertheless, our nitrogen isotope study indicates an oxic surface layer  
407 and availability of fixed N which may have played an important role in facilitating the  
408 evolution of eukaryotes since they are incapable of acquiring atmospheric  $\text{N}_2$  through  
409 N fixation.

410

#### 411 **ACKNOWLEDGMENTS**

412 This research is supported by the National Natural Science Foundation of China  
413 (41872032, 41830215, 41930320) and the Chinese ‘111’ project (B20011). X. Wang  
414 acknowledges the support from the China Scholarship Council for one-year of  
415 studying abroad. Thanks are given to Hao Yan for the kind help with the carbon and  
416 nitrogen isotope analyses and Tianyu Shen for help with sample collection. We  
417 appreciate Dr. Morrison Nolan for proofreading the paper. Valuable comments from  
418 Eva Stüeken and two anonymous reviewers improve the quality of this paper.

419

420 **REFERENCES CITED**

- 421 Ader, M., Macouin, M., Trindade, et al., 2009. A multilayered water column in the  
422 Ediacaran Yangtze platform? Insights from carbonate and organic matter paired  
423  $\delta^{13}\text{C}$ . *Earth and Planetary Science Letters*, 288: 213-227.  
424 <https://doi.org/10.1016/j.epsl.2009.09.024>
- 425 Ader, M., Sansjofre, P., Halverson, G.P., et al., 2014. Ocean redox structure across the  
426 Late Neoproterozoic Oxygenation Event: A nitrogen isotope perspective. *Earth  
427 and Planetary Science Letters*, 396: 1-13.  
428 <http://doi.org/10.1016/j.epsl.2014.03.042>
- 429 Ader, M., Thomazo, C., Sansjofre, P., et al., 2016. Interpretation of the nitrogen  
430 isotopic composition of Precambrian sedimentary rocks: Assumptions and  
431 perspectives. *Chemical Geology*, 429: 93-110.  
432 <http://doi.org/10.1016/j.chemgeo.2016.02.010>
- 433 Algeo, T.J., Meyers, P.A., Robinson, R.S., et al., 2014. Icehouse–greenhouse  
434 variations in marine denitrification. *Biogeosciences*, 11: 1273-1295.  
435 <https://doi.org/10.5194/bg-11-1273-2014>
- 436 Altabet, M.A., Pilskaln, C., Thunell, R., et al., 1999. The nitrogen isotope  
437 biogeochemistry of sinking particles from the margin of the Eastern North Pacific.  
438 *Deep Sea Research Part I: Oceanographic Research Papers*, 46: 655-679.  
439 [http://doi.org/10.1016/S0967-0637\(98\)00084-3](http://doi.org/10.1016/S0967-0637(98)00084-3)
- 440 Bristow, L.A., Dalsgaard, T., Tiano, L., et al., 2016. Ammonium and nitrite oxidation  
441 at nanomolar oxygen concentrations in oxygen minimum zone waters.

442 *Proceedings of the National Academy of Sciences*, 113: 10601-10606.  
443 <http://doi.org/10.1073/pnas.1600359113>

444 Canfield, D.E., Zhang, S., Frank, A.B., et al., 2018. Highly fractionated chromium  
445 isotopes in Mesoproterozoic-aged shales and atmospheric oxygen. *Nature*  
446 *Communications*, 9: 2871. <http://doi.org/10.1038/s41467-018-05263-9>

447 Chang, C., Hu, W., Wang, X., et al., 2019. Nitrogen isotope evidence for an  
448 oligotrophic shallow ocean during the Cambrian Stage 4. *Geochimica et*  
449 *Cosmochimica Acta*, 257: 49-67. <https://doi.org/10.1016/j.gca.2019.04.021>

450 Chen, Y., Diamond, C.W., Stüeken, E.E., et al., 2019. Coupled evolution of nitrogen  
451 cycling and redoxcline dynamics on the Yangtze Block across the  
452 Ediacaran-Cambrian transition. *Geochimica et Cosmochimica Acta*, 257: 243-265.  
453 <https://doi.org/10.1016/j.gca.2019.05.017>

454 Cole, D.B., Reinhard, C.T., Wang, X., et al., 2016. A shale-hosted Cr isotope record of  
455 low atmospheric oxygen during the Proterozoic. *Geology*, 44: 555-558.  
456 <http://doi.org/10.1130/g37787.1>

457 Crockford, P.W., Kunzmann, M., Bekker, A., et al., 2019. Claypool continued:  
458 Extending the isotopic record of sedimentary sulfate. *Chemical Geology*, 513:  
459 200-225. <https://doi.org/10.1016/j.chemgeo.2019.02.030>

460 Diamond, C.W., Planavsky, N.J., Wang, C., et al., 2018. What the ~1.4 Ga Xiamaling  
461 Formation can and cannot tell us about the mid-Proterozoic ocean. *Geobiology*,  
462 16: 219-236. <http://doi.org/doi:10.1111/gbi.12282>

463 Dong, L., Xiao, S., Shen, B., et al., 2008. Restudy of the worm-like carbonaceous

464 compression fossils Protoarenicola, Pararenicola, and Sinosabellidites from early  
465 Neoproterozoic successions in North China. *Palaeogeography,*  
466 *Palaeoclimatology, Palaeoecology*, 258: 138-161.  
467 <https://doi.org/10.1016/j.palaeo.2007.05.019>

468 Freudenthal, T., Wagner, T., Wenzhöfer, F., et al., 2001. Early diagenesis of organic  
469 matter from sediments of the eastern subtropical Atlantic: evidence from stable  
470 nitrogen and carbon isotopes. *Geochimica et Cosmochimica Acta*, 65: 1795-1808.  
471 [http://doi.org/10.1016/S0016-7037\(01\)00554-3](http://doi.org/10.1016/S0016-7037(01)00554-3)

472 Fuchsman, C.A., Murray, J.W., Konovalov, S.K., 2008. Concentration and natural  
473 stable isotope profiles of nitrogen species in the Black Sea. *Marine Chemistry*,  
474 111: 90-105. <http://doi.org/10.1016/j.marchem.2008.04.009>

475 Giblin, A.E., Tobias, C.R., Song, B., et al., 2013. The importance of dissimilatory  
476 nitrate reduction to ammonium (DNRA) in the nitrogen cycle of coastal  
477 ecosystems. *Oceanography*, 26 (3): 124–131.  
478 <https://doi.org/10.5670/oceanog.2013.54>

479 Godfrey, L.V., Poulton, S.W., Bebout, G.E., et al., 2013. Stability of the nitrogen cycle  
480 during development of sulfidic water in the redox-stratified late Paleoproterozoic  
481 Ocean. *Geology*, 41: 655-658. <http://doi.org/10.1130/g33930.1>

482 Guilbaud, R., Poulton, S.W., Butterfield, N.J., et al., 2015. A global transition to  
483 ferruginous conditions in the early Neoproterozoic oceans. *Nature Geosci*, 8:  
484 466-470. <http://doi.org/10.1038/ngeo2434>

485 Guilbaud, R., Poulton, S.W., Thompson, J., et al., 2020. Phosphorus-limited

486 conditions in the early Neoproterozoic ocean maintained low levels of  
487 atmospheric oxygen. *Nature Geoscience*, 13: 296-301.  
488 <http://doi.org/10.1038/s41561-020-0548-7>

489 Hayes, J.M., Strauss, H., Kaufman, A.J., 1999. The abundance of  $^{13}\text{C}$  in marine  
490 organic matter and isotopic fractionation in the global biogeochemical cycle of  
491 carbon during the past 800 Ma. *Chemical Geology*, 161: 103-125.  
492 [https://doi.org/10.1016/S0009-2541\(99\)00083-2](https://doi.org/10.1016/S0009-2541(99)00083-2)

493 Higgins, M.B., Robinson, R.S., Husson, J.M., et al., 2012. Dominant eukaryotic  
494 export production during ocean anoxic events reflects the importance of recycled  
495  $\text{NH}_4^+$ . *Proceedings of the National Academy of Sciences*, 109: 2269-2274.  
496 <http://doi.org/10.1073/pnas.1104313109>

497 Hong, T., Jia, Z., Yin, L., et al., 2004. Acritarchs from the Neoproterozoic Jiuliqiao  
498 Formation, Huainan region, and their biostratigraphic significance. *Acta*  
499 *Palaeontologica Sinica*, 43: 377–387.

500 Jiang, G., Wang, X., Shi, X., et al., 2012. The origin of decoupled carbonate and  
501 organic carbon isotope signatures in the early Cambrian (ca. 542–520 Ma)  
502 Yangtze platform. *Earth and Planetary Science Letters*, 317–318: 96-110.  
503 <https://doi.org/10.1016/j.epsl.2011.11.018>

504 Kipp, M.A., Stüeken, E.E., Yun, M., et al., 2018. Pervasive aerobic nitrogen cycling in  
505 the surface ocean across the Paleoproterozoic Era. *Earth and Planetary Science*  
506 *Letters*, 500: 117-126. <https://doi.org/10.1016/j.epsl.2018.08.007>

507 Knoll, A.H. and Nowak, M.A., 2017. The timetable of evolution. *Science Advances*, 3.

508 Koehler, M.C., Stüeken, E.E., Kipp, M.A., et al., 2017. Spatial and temporal trends in  
509 Precambrian nitrogen cycling: A Mesoproterozoic offshore nitrate minimum.  
510 *Geochimica et Cosmochimica Acta*, 198: 315-337.  
511 <https://doi.org/10.1016/j.gca.2016.10.050>

512 Lam, P., Kuypers, M.M.M., 2011. Microbial Nitrogen Cycling Processes in Oxygen  
513 Minimum Zones. *Annual Review of Marine Science*, 3: 317-345.  
514 <http://doi.org/10.1146/annurev-marine-120709-142814>

515 Lan, Z., Zhang, S., Tucker, M., et al., 2020. Evidence for microbes in early  
516 Neoproterozoic stromatolites. *Sedimentary Geology*, 398: 105-589.  
517 <https://doi.org/10.1016/j.sedgeo.2020.105589>

518 Lehmann, M.F., Bernasconi, S.M., Barbieri, A., et al., 2002. Preservation of organic  
519 matter and alteration of its carbon and nitrogen isotope composition during  
520 simulated and in situ early sedimentary diagenesis. *Geochimica et Cosmochimica*  
521 *Acta*, 66: 3573-3584. [http://doi.org/10.1016/S0016-7037\(02\)00968-7](http://doi.org/10.1016/S0016-7037(02)00968-7)

522 Li, G., Chen, L., Pang, K., et al., 2020. An assemblage of macroscopic and diversified  
523 carbonaceous compression fossils from the Tonian Shiwangzhuang Formation in  
524 western Shandong, North China. *Precambrian Research*, 346: 105801.  
525 <https://doi.org/10.1016/j.precamres.2020.105801>

526 Lu, W., Wörndle, S., Halverson, G.P., et al., 2017. Iodine proxy evidence for increased  
527 ocean oxygenation during the Bitter Springs Anomaly. *Geochemical Perspectives*  
528 *Letters*, 5: 53-57. <http://doi.org/10.7185/geochemlet.1746>

529 Luo, G., Junium, C.K., Izon, G., et al., 2018. Nitrogen fixation sustained productivity

530 in the wake of the Palaeoproterozoic Great Oxygenation Event. *Nature*  
531 *communications*, 9: 978. <http://doi.org/10.1038/s41467-018-03361-2>

532 Luo, G., Junium, C.K., Kump, L.R., et al., 2014. Shallow stratification prevailed for  
533 ~1700 to ~1300 Ma ocean: Evidence from organic carbon isotopes in the North  
534 China Craton. *Earth and Planetary Science Letters*, 400: 219-232.  
535 <http://doi.org/10.1016/j.epsl.2014.05.020>

536 Luo, G., Wang, Y., Algeo, T.J., et al., 2011. Enhanced nitrogen fixation in the  
537 immediate aftermath of the latest Permian marine mass extinction. *Geology*, 39:  
538 647-650. <https://doi.org/10.1130/g32024.1>

539 Lyons, T.W., Reinhard, C.T., Planavsky, N.J., 2014. The rise of oxygen in Earth's  
540 early ocean and atmosphere. *Nature*, 506: 307-315.  
541 <http://doi.org/10.1038/nature13068>

542 Macdonald, F.A., Schmitz, M.D., Crowley, J.L., et al., 2010. Calibrating the  
543 Cryogenian. *Science*, 327: 1241-1243. <https://doi.org/10.1126/science.1183325>

544 McCready R. G. L., Gould W. D., Barendregt R. W., 1983. Nitrogen isotope  
545 fractionation during the reduction of  $\text{NO}_3^-$  to  $\text{NH}_4^+$  by *Desulfovibrio sp.* *Can. J.*  
546 *Microbiol.*, 29: 231–234. <https://doi.org/10.1139/m83-038>

547 Michiels, C.C., Darchambeau, F., Roland, F.A.E., et al., 2017. Iron-dependent  
548 nitrogen cycling in a ferruginous lake and the nutrient status of Proterozoic  
549 oceans. *Nature Geoscience*, 10: 217. <https://doi.org/10.1038/ngeo2886>

550 Morales, L.V., Granger, J., Chang, B.X., et al., 2014. Elevated  $^{15}\text{N}/^{14}\text{N}$  in particulate  
551 organic matter, zooplankton, and diatom frustule-bound nitrogen in the

552 ice-covered water column of the Bering Sea eastern shelf. *Deep Sea Research*  
553 *Part II: Topical Studies in Oceanography* 109: 100-111.  
554 <https://doi.org/10.1016/j.dsr2.2014.05.008>

555 Ossa Ossa, F., Hofmann, A., Spangenberg, J.E., et al., 2019. Limited oxygen  
556 production in the Mesoarchean ocean. *Proceedings of the National Academy of*  
557 *Sciences*, 116: 6647-6652. <https://doi.org/10.1073/pnas.1818762116>

558 Pang, K., Tang, Q., Chen, L., et al., 2018. Nitrogen-Fixing Heterocystous  
559 Cyanobacteria in the Tonian Period. *Current Biology*, 28: 616-622.e611.  
560 <https://doi.org/10.1016/j.cub.2018.01.008>

561 Papineau, D., Purohit, R., Goldberg, T., et al., 2009. High primary productivity and  
562 nitrogen cycling after the Paleoproterozoic phosphogenic event in the Aravalli  
563 Supergroup, India. *Precambrian Research*, 171: 37-56.  
564 <http://doi.org/10.1016/j.precamres.2009.03.005>

565 Planavsky, N.J., 2014. The elements of marine life. *Nature Geosci*, 7: 855-856.  
566 <https://doi.org/10.1038/ngeo2307>

567 Planavsky, N.J., McGoldrick, P., Scott, C.T., et al., 2011. Widespread iron-rich  
568 conditions in the mid-Proterozoic ocean. *Nature*, 477: 448-451.  
569 <http://doi.org/10.1038/nature10327>

570 Planavsky, N.J., Reinhard, C.T., Wang, X., et al., 2014. Low Mid-Proterozoic  
571 atmospheric oxygen levels and the delayed rise of animals. *Science*, 346: 635-638.  
572 <http://doi.org/10.1126/science.1258410>

573 Planavsky, N.J., Cole, D.B., Reinhard, C.T., et al., 2016. No evidence for high

574 atmospheric oxygen levels 1,400 million years ago. *Proceedings of the National*  
575 *Academy of Sciences*, 113: E2550-E2551.  
576 <http://doi.org/10.1073/pnas.1601925113>

577 Poulton, S.W., Canfield, D.E., 2011. Ferruginous Conditions: A Dominant Feature of  
578 the Ocean through Earth's History. *Elements*, 7: 107-112.  
579 <https://doi.org/10.2113/gselements.7.2.107>

580 Prokopenko, M.G., Hammond, D.E., Berelson, W.M., et al., 2006. Nitrogen cycling in  
581 the sediments of Santa Barbara basin and Eastern Subtropical North Pacific:  
582 Nitrogen isotopes, diagenesis and possible chemosymbiosis between two  
583 lithotrophs (*Thioploca* and *Anammox*)—"riding on a glider". *Earth and*  
584 *Planetary Science Letters*, 242: 186-204.  
585 <http://doi.org/10.1016/j.epsl.2005.11.044>

586 Reinhard, C.T., Planavsky, N.J., Gill, B.C., et al., 2017. Evolution of the global  
587 phosphorus cycle. *Nature*, 541: 386-389. <http://doi.org/10.1038/nature20772>

588 Reinhard, C.T., Planavsky, N.J., Robbins, L.J., et al., 2013. Proterozoic ocean redox  
589 and biogeochemical stasis. *Proceedings of the National Academy of Sciences*, 110:  
590 5357-5362. <http://doi.org/10.1073/pnas.1208622110>

591 Riedman, L.A., Sadler, P.M., 2018. Global species richness record and  
592 biostratigraphic potential of early to middle Neoproterozoic eukaryote fossils.  
593 *Precambrian Research*, 319: 6-18.  
594 <https://doi.org/10.1016/j.precamres.2017.10.008>

595 Robinson, R.S., Kienast, M., Luiza Albuquerque, A., et al., 2012. A review of nitrogen

596 isotopic alteration in marine sediments. *Paleoceanography*, 27: PA4203.  
597 <http://doi.org/10.1029/2012pa002321>

598 Rooney, A.D., Macdonald, F.A., Strauss, J.V., et al., 2014. Re-Os geochronology and  
599 coupled Os-Sr isotope constraints on the Sturtian snowball Earth. *Proceedings of*  
600 *the National Academy of Sciences*, 111: 51-56.  
601 <https://doi.org/10.1073/pnas.1317266110>

602 Sahoo, S.K., Planavsky, N.J., Kendall, B., et al., 2012. Ocean oxygenation in the wake  
603 of the Marinoan glaciation. *Nature* 489: 546-549.  
604 <https://doi.org/10.1038/nature11445>

605 Scott, C., Lyons, T.W., Bekker, A., et al., 2008. Tracing the stepwise oxygenation of  
606 the Proterozoic ocean. *Nature*, 452: 456-U455.  
607 <http://doi.org/10.1038/nature06811>

608 Shang, M., Tang, D., Shi, X., et al., 2019. A pulse of oxygen increase in the early  
609 Mesoproterozoic ocean at ca. 1.57–1.56 Ga. *Earth and Planetary Science Letters*,  
610 527: 115797. <https://doi.org/10.1016/j.epsl.2019.115797>

611 Shen, B., Xiao, S., Zhou, C., et al., 2010. Carbon and sulfur isotope  
612 chemostratigraphy of the Neoproterozoic QuANJI Group of the Chaidam Basin,  
613 NW China: basin stratification in the aftermath of an Ediacaran glaciation  
614 postdating the Shuram event? *Precambrian Research*, 177: 241–252.  
615 <https://doi.org/10.1016/j.precamres.2009.12.006>

616 Sigman D. M., Karsh K. L., Casciotti K. L., 2009. Ocean Process Tracers: Nitrogen  
617 Isotopes in the Ocean. *Encyclopedia of Ocean Science*. Elsevier, Amsterdam, pp.

618 4138–4153.

619 Stüeken, E.E., 2013. A test of the nitrogen-limitation hypothesis for retarded  
620 eukaryote radiation: Nitrogen isotopes across a Mesoproterozoic basal profile.  
621 *Geochimica et Cosmochimica Acta*, 120: 121-139.  
622 <http://doi.org/10.1016/j.gca.2013.06.002>

623 Stüeken, E.E., Buick, R., Guy, B.M., et al., 2015. Isotopic evidence for biological  
624 nitrogen fixation by molybdenum-nitrogenase from 3.2 Gyr. *Nature*, 520:  
625 666-669. <https://doi.org/10.1038/nature14180>

626 Stüeken, E.E., Buick, R., Lyons, T.W., 2019. Revisiting the depositional environment  
627 of the Neoproterozoic Callanna Group, South Australia. *Precambrian Research*,  
628 334: 105474. <https://doi.org/10.1016/j.precamres.2019.105474>

629 Stüeken, E.E., Kipp, M.A., Koehler, M.C., et al., 2016. The evolution of Earth's  
630 biogeochemical nitrogen cycle. *Earth-Science Reviews*, 160: 220-239.  
631 <http://doi.org/10.1016/j.earscirev.2016.07.007>

632 Sun, W., Wang, G., Zhou, B., 1986. Macroscopic worm-like body fossils from the  
633 Upper Precambrian (900–700 Ma), Huainan district, Anhui, China and their  
634 stratigraphic and evolutionary significance. *Precambrian Research*, 31: 377–403.  
635 [https://doi.org/10.1016/0301-9268\(86\)90041-0](https://doi.org/10.1016/0301-9268(86)90041-0)

636 Tang, Q., Pang, K., Xiao, S., et al., 2013. Organic-walled microfossils from the early  
637 Neoproterozoic Liulaobei Formation in the Huainan region of North China and  
638 their biostratigraphic significance. *Precambrian Research*, 236: 157-181.  
639 <https://doi.org/10.1016/j.precamres.2013.07.019>

640 Tang, Q., Pang, K., Yuan, X. et al., 2017. Electron microscopy reveals evidence for  
641 simple multicellularity in the Proterozoic fossil *Chuarina*. *Geology* 45: 75-78.  
642 <https://doi.org/10.1130/g38680.1>

643 Tang, Q., Pang, K., Yuan, X., et al., 2020. A one-billion-year-old multicellular  
644 chlorophyte. *Nature Ecology & Evolution*, 4: 543-549.  
645 <http://doi.org/10.1038/s41559-020-1122-9>

646 Thomazo, C., Ader, M., Philippot, P., 2011. Extreme <sup>15</sup>N-enrichments in 2.72-Gyr-old  
647 sediments: evidence for a turning point in the nitrogen cycle. *Geobiology*, 9:  
648 107-120. <http://doi.org/10.1111/j.1472-4669.2011.00271.x>

649 Thomson, D., Rainbird, R.H., Planavsky, N., et al., 2015. Chemostratigraphy of the  
650 Shaler Supergroup, Victoria Island, NW Canada: A record of ocean composition  
651 prior to the Cryogenian glaciations. *Precambrian Research*, 263: 232-245.  
652 <https://doi.org/10.1016/j.precamres.2015.02.007>

653 Thunell, R.C., Sigman, D.M., Muller-Karger, F., et al., 2004. Nitrogen isotope  
654 dynamics of the Cariaco Basin, Venezuela. *Global Biogeochemical Cycles*, 18:  
655 GB3001. <http://doi.org/10.1029/2003gb002185>

656 Turner, E.C., Bekker, A., 2016. Thick sulfate evaporite accumulations marking a  
657 mid-Neoproterozoic oxygenation event (Ten Stone Formation, Northwest  
658 Territories, Canada). *Geological Society of America Bulletin*, 128: 203-222.  
659 <https://doi.org/10.1130/b31268.1>

660 Tyrrell, T., 1999. The relative influences of nitrogen and phosphorus on oceanic  
661 primary production. *Nature*, 400: 525-531. <https://doi.org/10.1038/22941>

662 Wang, D., Ling, H.-F., Struck, U., et al., 2018a. Coupling of ocean redox and animal  
663 evolution during the Ediacaran-Cambrian transition. *Nature Communications*, 9:  
664 2575. <http://doi.org/10.1038/s41467-018-04980-5>

665 Wang, G., Zhang, S., Li, S., et al., 1984. Research on the Upper Precambrian of  
666 Northern Jiangsu and Anhui Provinces. *Anhui Press of Science and Technology*,  
667 Hefei, Anhui, 1-209.

668 Wang, H., Zhang, Z., Li, C., et al., 2020a. Spatiotemporal redox heterogeneity and  
669 transient marine shelf oxygenation in the Mesoproterozoic ocean. *Geochimica et*  
670 *Cosmochimica Acta*, 270: 201-217. <https://doi.org/10.1016/j.gca.2019.11.028>

671 Wang, X., Jiang, G., Shi, X., et al., 2018b. Nitrogen isotope constraints on the early  
672 Ediacaran ocean redox structure. *Geochimica et Cosmochimica Acta*, 240:  
673 220-235. <https://doi.org/10.1016/j.gca.2018.08.034>

674 Wang, X., Shi, X., Tang, D., et al., 2013. Nitrogen Isotope Evidence for Redox  
675 Variations at the Ediacaran-Cambrian Transition in South China. *The Journal of*  
676 *Geology*, 121: 489-502. <http://doi.org/10.1086/671396>

677 Wang, Z., Wang, X., Shi, X., et al., 2020b. Coupled Nitrate and Phosphate Availability  
678 Facilitated the Expansion of Eukaryotic Life at Circa 1.56 Ga. *Journal of*  
679 *Geophysical Research: Biogeosciences*, 125: e2019JG005487.  
680 <https://doi.org/10.1029/2019jg005487>

681 Xiao, S., Shen, B., Tang, Q., et al., 2014. Biostratigraphic and chemostratigraphic  
682 constraints on the age of early Neoproterozoic carbonate successions in North  
683 China. *Precambrian Research*, 246: 208-225.

684 <https://doi.org/10.1016/j.precamres.2014.03.004>

685 Xiao, S., Bao, H., Wang, H., et al., 2004. The Neoproterozoic Quruqtagh Group in  
686 eastern Chinese Tianshan: evidence for a post-Marinoan glaciation. *Precambrian*  
687 *Res.*, 130: 1–26. <https://doi.org/10.1016/j.precamres.2003.10.013>

688 Xiao, S., Tang, Q., 2018. After the boring billion and before the freezing millions:  
689 evolutionary patterns and innovations in the Tonian Period. *Emerging Topics in*  
690 *Life Sciences*, 2: 161-171. <http://doi.org/10.1042/etls20170165>

691 Xing, Y., 1989. The Upper Precambrian of China, Volume 3 of “The Stratigraphy of  
692 China”. Geological Publishing House, Beijing: 1-314.

693 Xu, D., Wang, X., Shi, X., et al., 2020. Nitrogen cycle perturbations linked to  
694 metazoan diversification during the early Cambrian. *Palaeogeography,*  
695 *Palaeoclimatology,* *Palaeoecology,* 538: 109392.  
696 <https://doi.org/10.1016/j.palaeo.2019.109392>

697 Yang, D.B., Xu, W.L., Xu, Y.G., et al., 2012. U–Pb ages and Hf isotope data from  
698 detrital zircons in the Neoproterozoic sandstones of northern Jiangsu and  
699 southern Liaoning Provinces, China: implications for the late Precambrian  
700 evolution of the southeastern North China Craton. *Precambrian Res.*, 216–219:  
701 162–176. <https://doi.org/10.1016/j.precamres.2012.07.002>

702 Yin, C., 1985. Micropaleoflora from the Late Precambrian in Huainan region of Anhui  
703 Province and its stratigraphic significance. *Professional Papers of Stratigraphy*  
704 *and Palaeontology*, Chinese Academy of Geological Sciences, 12: 97–119.

705 Yin, L., Sun, W., 1994. Microbiota from Neoproterozoic Liulaobei Formation in the

706 Huainan region, Northern Anhui, China. *Precambrian Research*, 65: 95–114.  
707 [https://doi.org/10.1016/0301-9268\(94\)90101-5](https://doi.org/10.1016/0301-9268(94)90101-5)

708 Zang, W., Walter, M.R., 1992. Late Proterozoic and Early Cambrian microfossils and  
709 biostratigraphy, northern Anhui and Jiangsu, central-eastern China. *Precambrian*  
710 *Research*, 57: 243–323. [https://doi.org/10.1016/0301-9268\(92\)90004-8](https://doi.org/10.1016/0301-9268(92)90004-8)

711 Zerkle, A.L., Poulton, S.W., Newton, R.J., et al., 2017. Onset of the aerobic nitrogen  
712 cycle during the Great Oxidation Event. *Nature*, 542: 465-467.  
713 <http://doi.org/10.1038/nature20826>

714 Zhang, K., Zhu, X., Wood, R.A., et al., 2018. Oxygenation of the Mesoproterozoic  
715 ocean and the evolution of complex eukaryotes. *Nature Geoscience*, 11: 345-350.  
716 <http://doi.org/10.1038/s41561-018-0111-y>

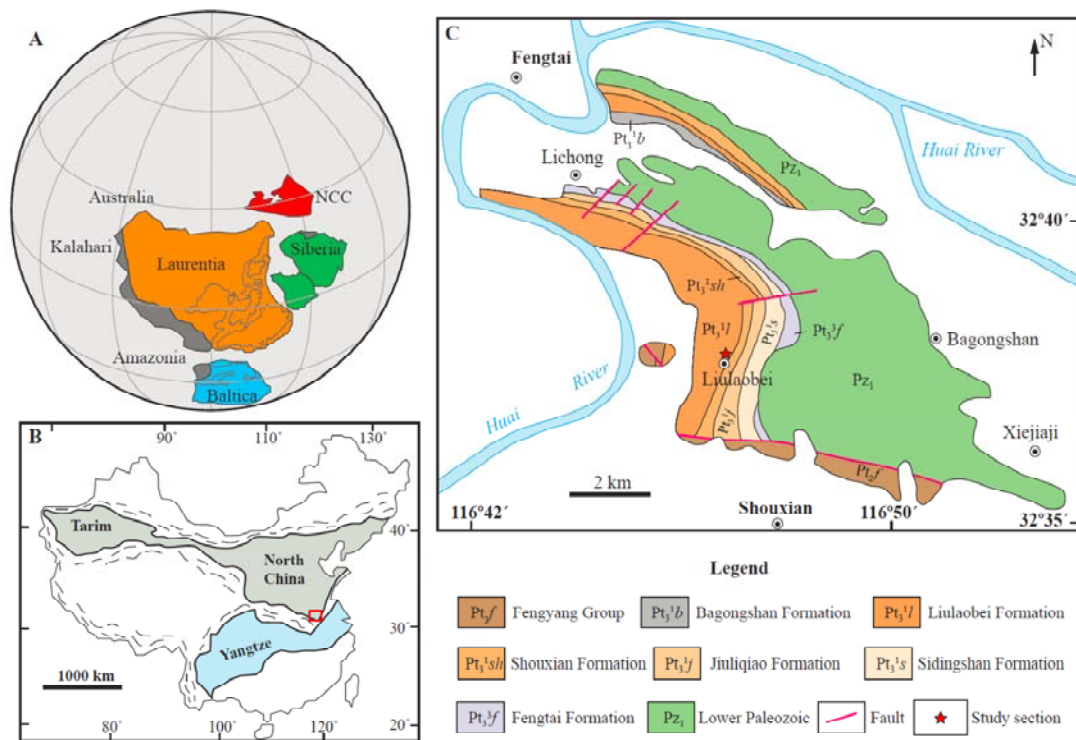
717 Zhang, S.C., Wang, X.M., Wang, H.J., et al., 2016. Sufficient oxygen for animal  
718 respiration 1,400 million years ago. *Proceedings of the National Academy of*  
719 *Sciences of the United States of America*, 113: 1731-1736.  
720 <http://doi.org/10.1073/pnas.1523449113>

721 Zhang, X., Sigman, D.M., Morel, F.M.M. et al., 2014. Nitrogen isotope fractionation  
722 by alternative nitrogenases and past ocean anoxia. *Proceedings of the National*  
723 *Academy of Sciences*, 111: 4782-4787. <http://doi.org/10.1073/pnas.1402976111>

724 Zhao, H., Zhang, S., Ding, J., et al., 2020. New geochronologic and paleomagnetic  
725 results from early Neoproterozoic mafic sills and late Mesoproterozoic to early  
726 Neoproterozoic successions in the eastern North China Craton, and implications

727 for the reconstruction of Rodinia. *GSA Bulletin*, 132: 739-766.

728 <https://doi.org/10.1130/b35198.1>



730

731 Fig. 1 (A) Paleogeographic position of the North China Craton in Rodinia during the

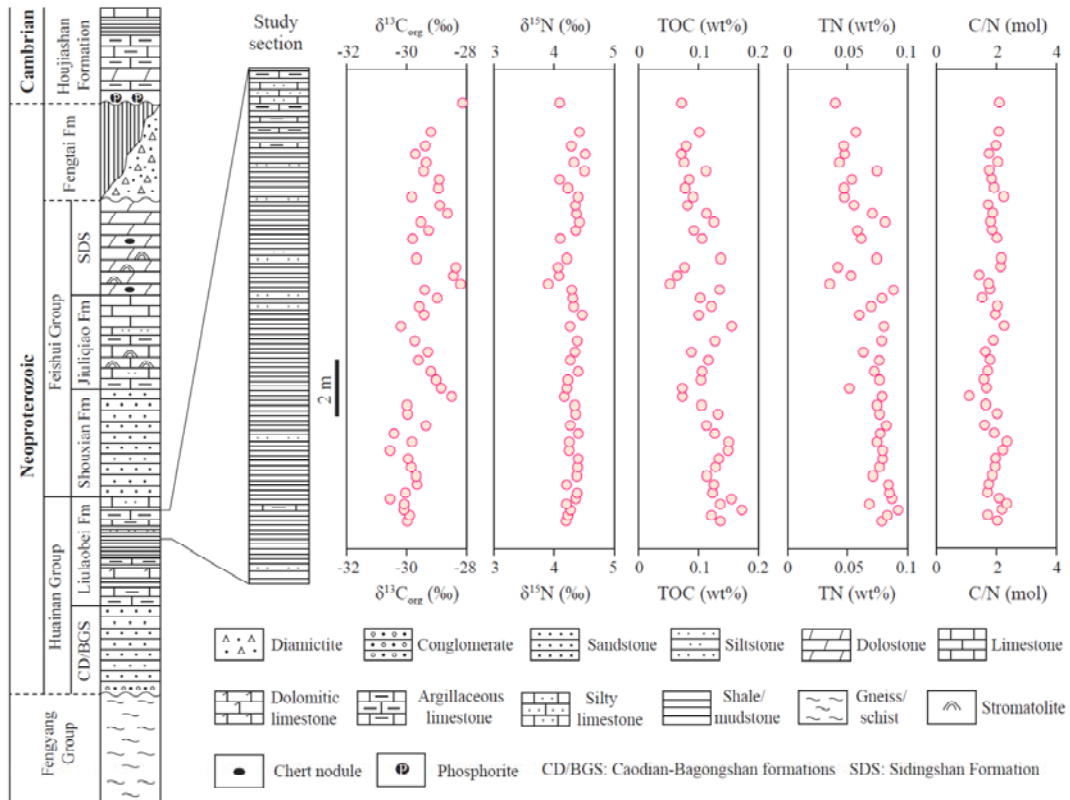
732 early Neoproterozoic (Zhao et al., 2020). (B) Tectonic outline showing the major

733 blocks in China. The red rectangle shows the location of the study area. (C)

734 Simplified geological map of the study area in Huainan, modified from Zhao et al.

735 (2020). The red star shows the location of the study section.

736



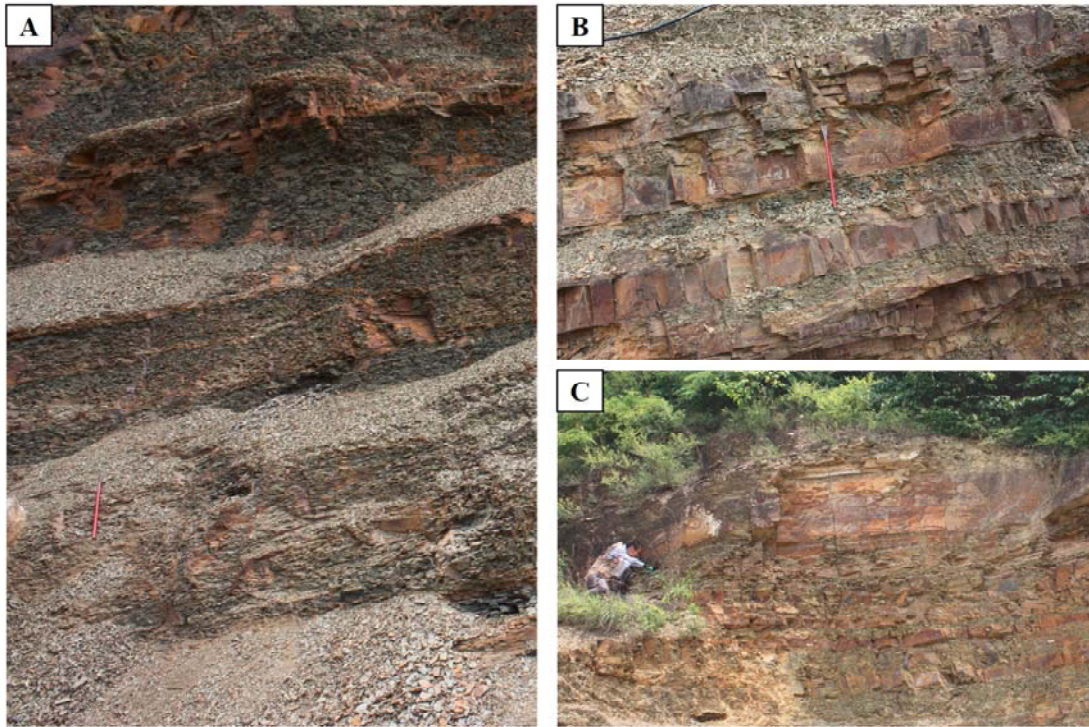
737

738 Fig. 2 Geochemical profiles of  $\delta^{13}\text{C}_{\text{org}}$ ,  $\delta^{15}\text{N}$ , TOC, TN, and C/N in the study section.

739 The stratigraphic column of the Neoproterozoic succession is revised from Tang

740 et al. (2013) and is not scaled according to the scale of thickness.

741



742

743 Fig. 3 Macroscopic field photos showing the major lithology of the study section. (A)

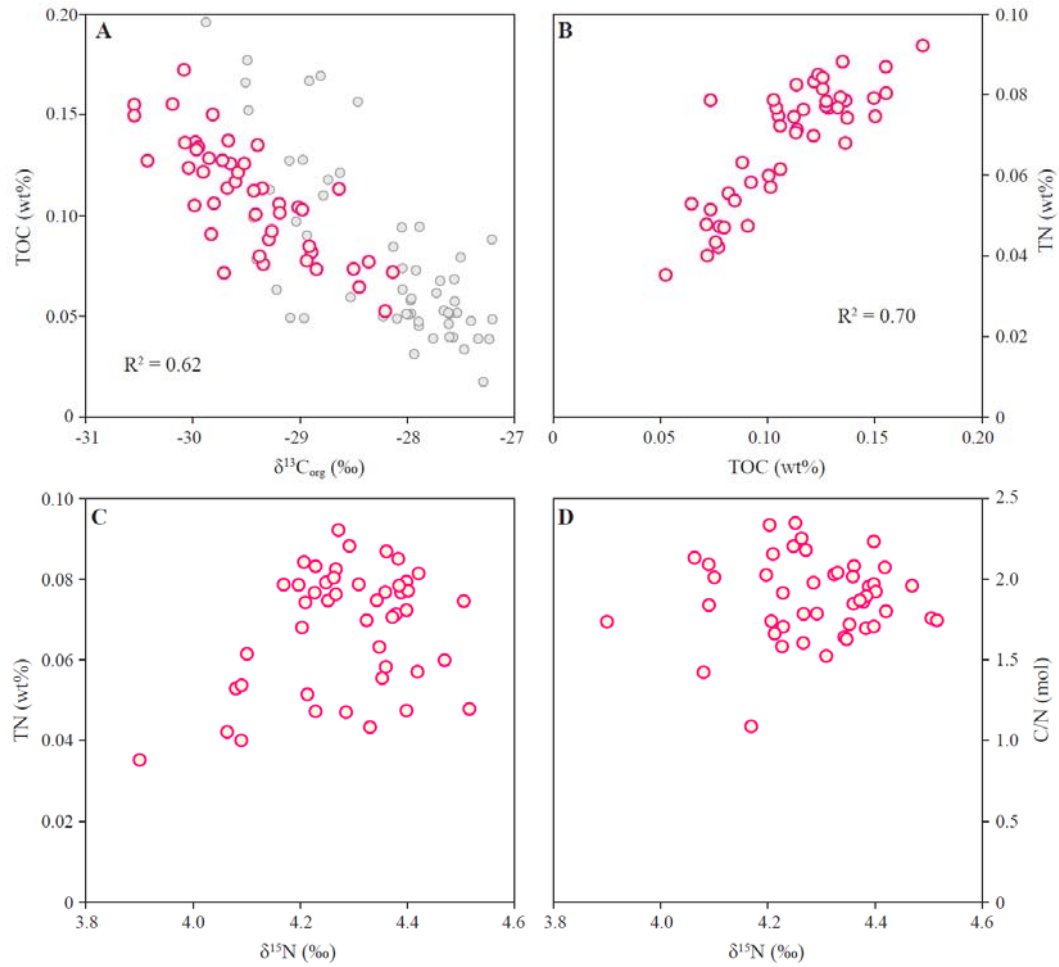
744 The gray greenish shale in the lower part of the study section. (B) Interbedded

745 siltstone and shale in the middle part of the study section. The red chisel in A and B is

746 about 30 cm long. (C) Medium to thick argillaceous limestone intercalated with shale

747 in the upper part of the study section.

748

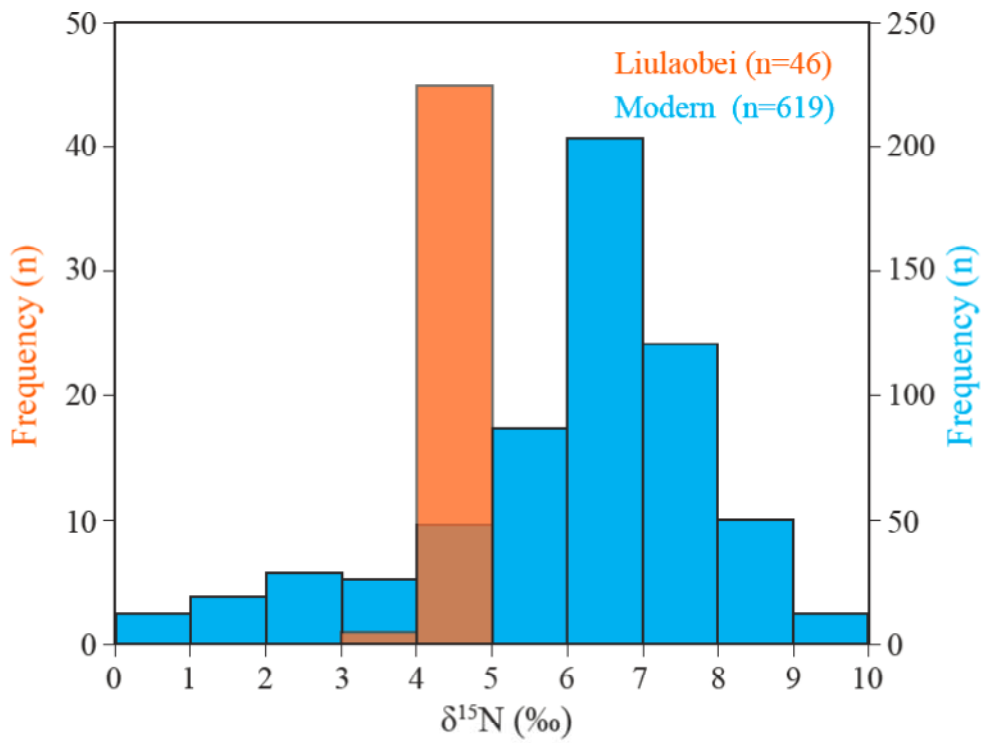


749

750 Fig. 4 Cross-plots of TOC vs.  $\delta^{13}C_{org}$  (A), TOC vs. TN (B), TN vs.  $\delta^{15}N$  (C), and C/N

751 vs.  $\delta^{15}N$  (D). The data in gray circles are from Guilbaud et al. (2020).

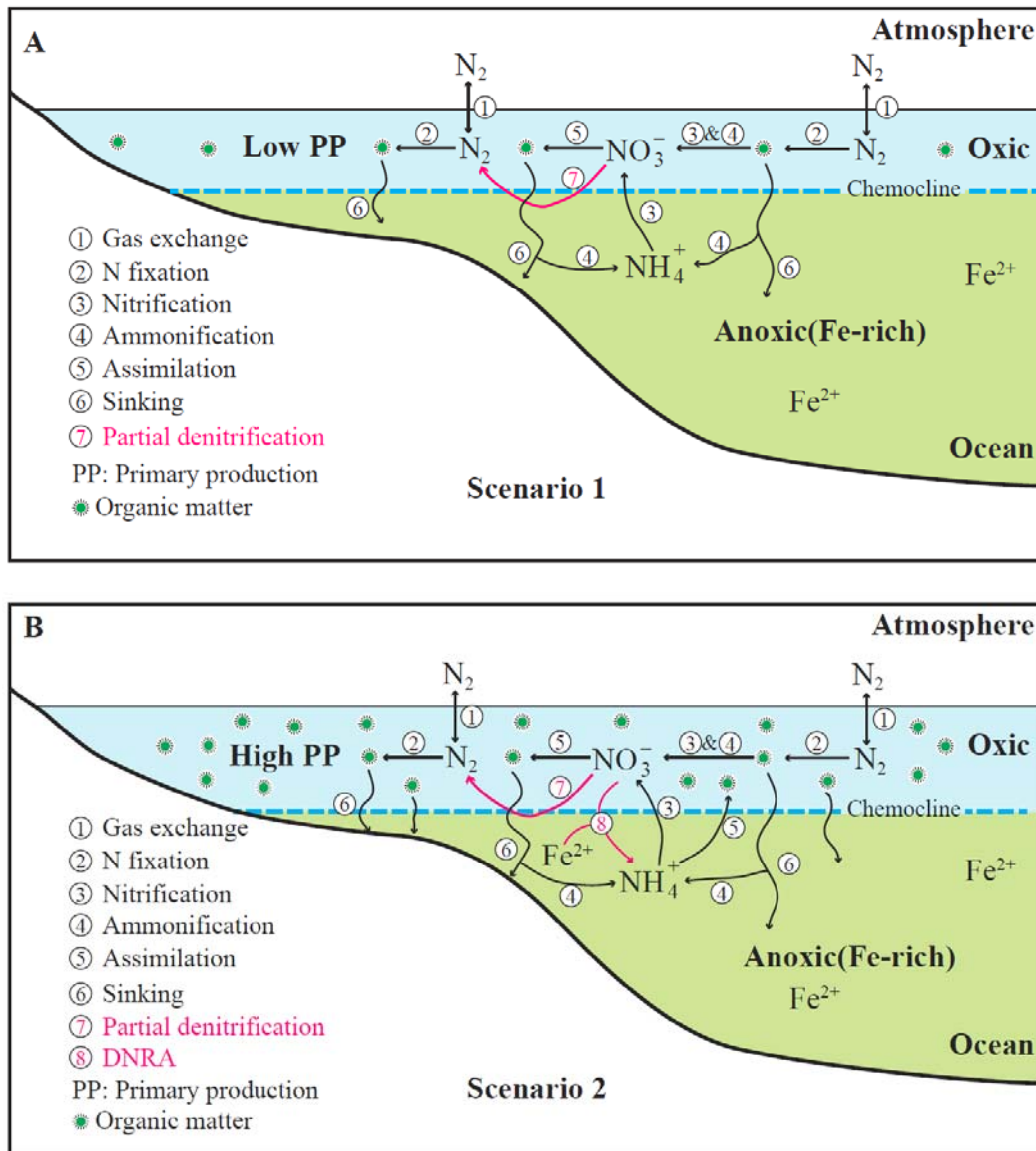
752



753

754 Fig. 5 The correlation of the  $\delta^{15}\text{N}$  distribution in the Liulaobei Formation with modern  
 755 sediments. The  $\delta^{15}\text{N}$  data for the modern sediments are from the compilation of Kipp  
 756 et al. (2018).

757



758

759 Fig. 6 Schematic diagrams illustrating the biogeochemical nitrogen cycling during the  
 760 early Neoproterozoic in North China. Two scenarios may explain the observed  $\delta^{15}\text{N}$   
 761 records in the Liulaobei Formation. In scenario 1 (A), the positive  $\delta^{15}\text{N}$  values are  
 762 attributed to partial denitrification in the stratified ocean due to low primary  
 763 production by P limitation (Guilbaud et al., 2020). In scenario 2 (B), denitrification  
 764 coupled with DNRA may be responsible for the positive  $\delta^{15}\text{N}$  in the Liulaobei  
 765 Formation (see the detailed explanation in the main text).

766

**Table A1: Nitrogen and organic carbon isotope data from the Liulaobei Formation**

Sample	Height (m)	Lithology	$\delta^{13}\text{C}_{\text{org}}$ (‰)	TOC (wt %)	$\delta^{15}\text{N}$ (‰)	TN (wt %)	C/N (mol)
LLB-0	0.0	Gray shale	-29.98	0.14	4.20	0.08	2.03
LLB-0.2	0.2	Gray shale	-29.90	0.12	4.23	0.08	1.70
LLB-0.4	0.4	Gray shale	-30.08	0.17	4.27	0.09	2.18
LLB-0.6	0.6	Gray shale	-30.07	0.14	4.20	0.07	2.34
LLB-0.8	0.8	Gray shale	-30.55	0.16	4.36	0.09	2.08
LLB-1.0	1.0	Gray shale	-30.04	0.12	4.38	0.09	1.70
LLB-1.3	1.3	Gray shale	-29.65	0.13	4.21	0.08	1.74
LLB-1.6	1.6	Gray shale	-29.68	0.11	4.38	0.07	1.86
LLB-1.9	1.9	Gray shale	-29.85	0.13	4.39	0.08	1.95
LLB-2.2	2.2	Gray shale	-29.95	0.13	4.40	0.08	1.97
LLB-2.5	2.5	Gray shale	-30.55	0.15	4.25	0.08	2.20
LLB-2.8	2.8	Gray shale	-29.81	0.15	4.25	0.07	2.35
LLB-3.1	3.1	Gray shale	-30.42	0.13	4.40	0.08	1.92
LLB-3.4	3.4	Gray shale	-29.35	0.11	4.27	0.08	1.61
LLB-3.8	3.8	Gray shale	-29.97	0.13	4.36	0.08	2.02
LLB-4.1	4.1	Gray shale	-29.98	0.11	4.34	0.07	1.64
LLB-4.4	4.4	Gray shale	-28.50	0.07	4.17	0.08	1.09
LLB-4.7	4.7	Gray shale	-28.85	0.07	4.21	0.05	1.66
LLB-5.0	5.0	Gray shale	-29.02	0.10	4.23	0.08	1.58
LLB-5.3	5.3	Gray shale	-29.20	0.11	4.40	0.07	1.71
LLB-5.7	5.7	Gray shale	-29.60	0.12	4.27	0.08	1.78
LLB-6.0	6.0	Gray shale	-29.29	0.09	4.35	0.06	1.63
LLB-6.4	6.4	Gray shale	-29.72	0.13	4.38	0.08	1.90
LLB-6.9	6.9	Gray shale	-30.19	0.16	4.26	0.08	2.25
LLB-7.3	7.3	Gray shale	-29.41	0.10	4.47	0.06	1.96
LLB-7.6	7.6	Gray shale	-29.58	0.12	4.32	0.07	2.03
LLB-7.9	7.9	Gray shale	-28.98	0.10	4.31	0.08	1.52
LLB-8.2	8.2	Gray shale	-29.40	0.14	4.29	0.09	1.79
LLB-8.4	8.4	Gray shale	-28.21	0.05	3.90	0.04	1.74
LLB-8.7	8.7	Gray shale	-28.45	0.06	4.08	0.05	1.42
LLB-9.0	9.0	Gray shale	-28.36	0.08	4.06	0.04	2.13
LLB-9.3	9.3	Gray shale	-29.67	0.14	4.21	0.07	2.16
LLB-10.0	10.0	Gray shale	-29.80	0.11	4.10	0.06	2.01
LLB-10.3	10.3	Gray shale	-29.26	0.09	4.36	0.06	1.85
LLB-10.6	10.6	Gray shale	-29.52	0.13	4.42	0.08	1.80
LLB-10.9	10.9	Gray shale	-28.64	0.11	4.37	0.07	1.87
LLB-11.2	11.2	Gray shale	-28.89	0.08	4.35	0.06	1.72
LLB-11.5	11.5	Gray shale	-29.83	0.09	4.40	0.05	2.23
LLB-11.8	11.8	Gray shale	-28.94	0.08	4.23	0.05	1.91
LLB-12.1	12.1	Gray shale	-28.92	0.08	4.09	0.05	1.84
LLB-12.4	12.4	Gray shale	-29.43	0.11	4.51	0.07	1.76
LLB-12.7	12.7	Gray shale	-29.34	0.08	4.33	0.04	2.04

LLB-13.0	13.0	Gray shale	-29.71	0.07	4.52	0.05	1.75
LLB-13.3	13.3	Gray shale	-29.38	0.08	4.29	0.05	1.98
LLB-13.8	13.8	Gray shale	-29.19	0.10	4.42	0.06	2.07
LLB-14.8	14.8	Gray shale	-28.14	0.07	4.09	0.04	2.09

---